International Journal of Mechanical Sciences 278 (2024) 109443

Contents lists available at ScienceDirect

International Journal of Mechanical Sciences

journal homepage: www.elsevier.com/locate/ijmecsci

Modeling of martensitic phase transformation accounting for inertia effects

Xiaoying Liu [a,*], Daniel Schneider [a,c], Martin Reder [b,c], Paul W. Hoffrogge [a,c], Britta Nestler [a,b,c]

[a] Institute of Nanotechnology (INT-MSS), Karlsruhe Institute of Technology, Karlsruhe, 76131, Germany
[b] Institute for Applied Materials (IAM-MMS), Karlsruhe Institute of Technology, Karlsruhe, 76131, Germany
[c] Institute for Digital Materials Science (IDM), Karlsruhe University of Applied Sciences, 76133, Germany

ARTICLE INFO

Keywords:
Martensitic phase transformation
Multiphase-field modeling
Dynamic mechanics
Transformation strain
Phase transformation velocity
Inertia effects

ABSTRACT

As a diffusionless phase transformation, martensite evolves at the speed close to sound, with its kinetics and morphology dominated by the mechanical energy. However, the mechanism of martensitic phase transformation with the consideration of inertia is rarely investigated. This paper presents a multiphase-field model, where the transformation strain in martensite performs as the mechanical wave source, and in return the kinetic energy contributes to the driving force for phase transformation. As a result, the mechanical fields, i.e., the stress and the velocity, are derived according to the increment of the transformation strain. The propagation direction of the mechanical wave is corrected by considering the growth of the martensitic nucleus. With the 1D and 2D analysis, as well as the comparison against 2D static case, the mechanism of martensitic phase transformation is investigated, and the advantage of mechanical model accounting for inertia effects is illustrated.

1. Introduction

Martensitic steel is often used in industrial production, medical treatment and shipping, due to its advantages in terms of strength, hardness and corrosion resistance [1–5]. Martensite is formed from austenite during quenching, which results in a diffusionless phase transformation. This is a rapid displacive phase transformation that takes place close to the speed of sound [6–8]. Clapp [9] pointed out that the kinetics and morphology of the martensitic phase transformation are dominated by the mechanical energy and defined that *"A martensitic transformation involves a cooperative motion of a set of atoms across an interface causing a shape change and sound."*. In a macroscopic specimen subjected to impact loading, Xiao et al. [10] found that the initial transformation front propagated at a speed of about 2.3 km/s, i.e., the elastic wave speed in austenite, and decreased to 0.7 km/s and finally to 0.58 km/s. Planes et al. [11] collected and analyzed the acoustic emission resulting from the sudden local displacement at the transformation front, during the martensitic phase transformation. Schwabe et al. [12] reported that martensitic phase transformation completed within hundreds of ns for a film with the thickness of 500 nm, during which the limitation of heat dissipation exists. From the time scale perspective, a mechanical model accounting for inertia effects can be established in which the martensitic phase transformation acts as a mechanical wave source and, in turn, the kinetic energy contributes to the driving force for the phase transformation.

In Kashchenko et al. [13,14], a dynamic model with a control wave process was proposed to analyze the formation of martensitic crystals. Molecular Dynamics (MD) simulation was used to observe the martensitic transformation after a compressive shock wave [15,16]. Wei et al. [17] also used the MD method to simulate high-speed martensitic phase transformation. The phase-field modeling, which derives the driving force for the evolution of order parameters based on the free energy functions, has been developed rapidly in recent decades, due to its great advantages in reducing the large amount of effort in tracking the interface [18–23]. This material microstructure modeling approach is widely used in the simulation of solidification [24–26], flow [27–29], fracture [30–32], composite material [33–35], battery [36–38], and so on. Martensitic phase transformation is also widely investigated by the phase-field modeling. Basak and Levitas [39], Tuma et al. [40] and Babaei and Levitas [41] simulated martensitic phase transformation with finite strain. The interfacial tension during multivariant martensitic phase transformation is also studied [42–44]. Xu and Kang [45], Xu et al. [46] investigated the superelasticity property of NiTi alloy during the martensitic phase transformation. Ahluwalia et al. [47], Zhang et al. [48] and Mo et al. [49] analyzed the plasticity induced by martensitic phase transformation. The phase-field modeling is also used to simulate the different stages of phase transformation for shape memory alloy under different loading conditions [50–54]. Furthermore, the martensitic phase transformation is also studied together with magnetics [55–57]. Jafarzadeh et al. [58] investigated

* Corresponding author.
E-mail address: xiaoying.liu@kit.edu (X. Liu).

https://doi.org/10.1016/j.ijmecsci.2024.109443
Received 22 February 2024; Received in revised form 8 May 2024; Accepted 30 May 2024
Available online 6 June 2024

the interaction between martensitic phase transformation and fracture through analyzing the surface energy. Amirian et al. [59] presented the evolution of twinning and fracture by solving the Ginzburg–Landau-based phase-field theory and the mechanical equilibrium equation with the finite element method. Cui et al. [60] reported the influence of grain size on the martensitic morphology by considering the strain accommodation. Rezaee-Hajidehi and Stupkiewicz [61] studied the size effect in nano-indentation during multivariant martensitic phase transformation through analyzing the interfacial energy. Cho et al. [62] and Idesman et al. [63] analyzed the influence of inertial forces on martensitic phase transformation, and proved that the occurring of martensitic phase transformation is of the order of magnitude of 1 ps. However, to the authors' knowledge, a detailed analysis of the mechanism for martensitic phase transformation and an insight into the interaction between martensitic phase transformation and kinetic energy are still missing.

For the phase-field modeling involving solid mechanics, several homogenization methods have been proposed to interpolate the mechanical fields at the diffuse interface. The most commonly used methods are the Voigt/Taylor (VT) model [64,65], the Reuss/Sachs (RS) model[66,67] and the Khachaturyan (KH) model [68,69]. The VT and RS models respectively assume identical strains and stresses across the diffuse interface, while the KH model can be considered as a combination of the VT and RS models [70]. However, excess interfacial energy is generated by all these three methods [71]. In order to correct the interfacial energy, Schneider et al. [72] derived the formula for the effective stiffness matrix and the stress tensor according to the balance conditions at the sharp interface. Schöller et al. [73] and Herrmann et al. [74] have applied this balance-condition-based homogenization scheme to simulate crack propagation. Herrmann et al. [75] utilized it to study the elasto-plasticity property during martensitic phase transformation. Liu et al. [76] further developed this derivation procedure for dynamic mechanics and carried out the corresponding parameter study in Liu et al. [77]. The dynamic mechanical model in Liu et al. [76] is further developed in this paper, where the martensitic phase transformation acts as a mechanical wave source and the kinetic energy in return contributes to the driving force for the phase transformation.

The remaining part of this paper is organized as follows. The multiphase-field model is presented in Section 2, where the order parameter ϕ_α for each phase/grain evolves according to the partial derivative of the total free energy and the noise. Section 3 introduces the mechanical model accounting for inertia effects within the framework of multiphase-field method. Specifically, it presents the governing equation for mechanical wave, derives the increment of the stress, the elastic strain and the velocity fields, and corrects the formula for the mechanical fields by considering the direction of the mechanical wave propagation. Numerical validations in 1D and 2D are analyzed in Section 4 to verify the phase-field modeling coupled with dynamic mechanics. The 2D results are also compared with those from phase-field modeling in conjunction with static mechanics. Last but not least, conclusions are addressed in Section 5.

2. Multiphase-field model

In the multiphase-field model, the order parameter ϕ_α represents the volume fraction of the phase/grain α. For a system with N order parameters, the constraint $\sum_\alpha^N \phi_\alpha = 1 \ \ (0 \le \phi_\alpha \le 1)$ should be satisfied from the physical point of view. With the N-tuples $\boldsymbol{\phi} = (\phi_1, \phi_2, \dots, \phi_N)$, the total free energy $\mathcal{F}$ is expressed as [78,79]:

$$\mathcal{F} = \int_V \left(\epsilon a(\boldsymbol{\nabla\phi}) + \frac{1}{\epsilon}\omega(\boldsymbol{\phi}) + f_{chem}(\boldsymbol{\phi}) + f_d(\boldsymbol{\phi},\boldsymbol{\varepsilon},\boldsymbol{v}) \right) \mathrm{d}V, \tag{1}$$

where ∇ is the gradient operator and V denotes the total volume of the simulated domain.

According to Steinbach and Pezzolla [80], supposing $\gamma_{\alpha\beta}$ is the $\alpha-\beta$ interfacial energy, the gradient energy density $a(\boldsymbol{\nabla\phi})$ reads:

$$a(\boldsymbol{\nabla\phi}) = -\sum_{\alpha,\beta>\alpha} \gamma_{\alpha\beta} \nabla\phi_\alpha \nabla\phi_\beta, \tag{2}$$

and the potential energy density $\omega(\boldsymbol{\phi})$ takes the form [78]:

$$\omega(\boldsymbol{\phi}) = \frac{16}{\pi^2} \sum_{\alpha,\beta>\alpha} \gamma_{\alpha\beta}\phi_\alpha\phi_\beta. \tag{3}$$

Nestler et al. [78] added the high-order term $\gamma_{\alpha\beta\delta}\phi_\alpha\phi_\beta\phi_\delta$ to Eq. (3) to avoid the appearance of the artificial third phase in the two-phase region. Daubner et al. [81] proved that the combination of Eqs. (2) and (3) can also suppress the occurrence of the artificial third phase. In the multiphase-field model, the sharp interface between different phases/grains is approximated by the diffuse interface. ϵ is a parameter related to the thickness of the diffuse interface. If only the interfacial energy is considered, i.e., $a(\boldsymbol{\nabla\phi})$ and $\omega(\boldsymbol{\phi})$, it can be deduced that the diffuse interfacial width in the equilibrium state is $L = \epsilon\pi^2/4$.

In Eq. (1), $f_{chem}(\boldsymbol{\phi})$ is the chemical energy density, which is equal to f_{chem}^α in the bulk region $\phi_\alpha = 1$ and is continuously interpolated across the diffuse interface region $0 < \phi_\alpha < 1$. Thus, $f_{chem}(\boldsymbol{\phi})$ is calculated as:

$$f_{chem}(\boldsymbol{\phi}) = \sum_\alpha f_{chem}^\alpha h(\phi_\alpha), \tag{4}$$

where $h(\phi_\alpha)$ is a continuous interpolation function, which satisfies the requirement $\sum_\alpha h(\phi_\alpha) = 1 \ (0 \le h(\phi_\alpha) \le 1)$. $h(\phi_\alpha)$ can be calculated with $\boldsymbol{\phi}$ in different ways, as shown in Schneider et al. [79]. In this paper, $h(\phi_\alpha) = \phi_\alpha$, and f_{chem}^α is constant for each phase α.

With $\boldsymbol{\varepsilon}$ and $\boldsymbol{v}$ respectively representing the infinitesimal strain tensor in the Voigt notation and the material particle velocity vector, $f_d(\boldsymbol{\phi},\boldsymbol{\varepsilon},\boldsymbol{v})$ in Eq. (1) denotes the kinetic energy density, which is divided into two parts, i.e., the elastic energy density $f_\varepsilon(\boldsymbol{\phi},\boldsymbol{\varepsilon})$ and the kinetic energy density $f_v(\boldsymbol{\phi},\boldsymbol{v})$. Similar to $f_{chem}(\boldsymbol{\phi})$, $f_d(\boldsymbol{\phi},\boldsymbol{\varepsilon},\boldsymbol{v})$ is expressed as an interpolation of all phase contributions:

$$f_d(\boldsymbol{\phi},\boldsymbol{\varepsilon},\boldsymbol{v}) = \sum_\alpha f_d^\alpha(\boldsymbol{\varepsilon}^\alpha,\boldsymbol{v}^\alpha) h(\phi_\alpha) = \underbrace{\sum_\alpha f_\varepsilon^\alpha(\boldsymbol{\varepsilon}^\alpha) h(\phi_\alpha)}_{f_\varepsilon(\boldsymbol{\phi},\boldsymbol{\varepsilon})} + \underbrace{\sum_\alpha f_v^\alpha(\boldsymbol{v}^\alpha) h(\phi_\alpha)}_{f_v(\boldsymbol{\phi},\boldsymbol{v})}. \tag{5}$$

The derivation of $f_d(\boldsymbol{\phi},\boldsymbol{\varepsilon},\boldsymbol{v})$ and its contribution in the process of phase transformation will be presented in detail in Sections 3 and 4.

Based on Eq. (1), the evolution process of each phase/grain α can be simulated through the evolution of the order parameter ϕ_α, which is derived as [82]:

$$\frac{\partial\phi_\alpha}{\partial t} = -\frac{1}{\tilde{N}\epsilon} \sum_\beta^{\tilde{N}} M_{\alpha\beta} \left[\underbrace{\frac{\delta\mathcal{F}_{intf}}{\delta\phi_\alpha} - \frac{\delta\mathcal{F}_{intf}}{\delta\phi_\beta} + \frac{8\sqrt{\phi_\alpha\phi_\beta}}{\pi} \left(\frac{\delta\mathcal{F}_{bulk}}{\delta\phi_\alpha} - \frac{\delta\mathcal{F}_{bulk}}{\delta\phi_\beta} \right)}_{I} + \epsilon\Delta\hat{a}_{\alpha\beta} \right] + \frac{\partial\zeta}{\partial\phi_\alpha}, \tag{6}$$

where t denotes the time variable, while $\tilde{N}$ is the number of local active phases. $M_{\alpha\beta}$ is the mobility for the $\alpha-\beta$ interface. $\mathcal{F} = \mathcal{F}_{intf} + \mathcal{F}_{bulk}$, with $\mathcal{F}_{intf}$ referring to the volumetric integration of the interfacial energy $a(\boldsymbol{\nabla\phi})$ and $\omega(\boldsymbol{\phi})$, while $\mathcal{F}_{bulk}$ contains the volumetric integration of the bulk energy $f_{chem}(\boldsymbol{\phi})$ and $f_d(\boldsymbol{\phi},\boldsymbol{\varepsilon},\boldsymbol{v})$.

In Eq. (6), $\delta\mathcal{F}_{intf}/\delta\phi_\alpha$ is calculated as:

$$\frac{\delta\mathcal{F}_{intf}}{\delta\phi_\alpha} = \left(\frac{\partial}{\partial\phi_\alpha} - \nabla\cdot\frac{\partial}{\partial\boldsymbol{\nabla}\phi_\alpha} \right) \left(\epsilon a(\boldsymbol{\nabla\phi}) + \frac{1}{\epsilon}\omega(\boldsymbol{\phi}) \right), \tag{7}$$

where $\nabla\cdot$ represents the divergence operator. A similar operation applies to $\delta\mathcal{F}_{intf}/\delta\phi_\beta$, $\delta\mathcal{F}_{bulk}/\delta\phi_\alpha$ and $\delta\mathcal{F}_{bulk}/\delta\phi_\beta$ in Eq. (6). Steinbach [82] pointed out that part I in Eq. (6) can result in correct interfacial kinetics, when using the obstacle-type potential energy, i.e., Eq. (3) together with $h(\phi_\alpha) = \phi_\alpha$.

In Eq. (6), the term $\epsilon\Delta\hat{a}_{\alpha\beta} = \epsilon\left(\hat{a}\left(\nabla\phi_\alpha\right) - \hat{a}\left(\nabla\phi_\beta\right)\right)$ is inserted, with

$$\hat{a}\left(\nabla\phi_\alpha\right) = \gamma_\alpha^c\left(\nabla^2\phi_\alpha - |\nabla\phi_\alpha|\nabla\cdot\frac{\nabla\phi_\alpha}{|\nabla\phi_\alpha|}\right). \tag{8}$$

where γ_α^c is a parameter to numerically stabilize the interface, and does not contribute to the interfacial driving force. For detailed derivation and discussion please refer to Selzer [83] and Schoof et al. [84].

For a correct interaction between gradient and potential energy density, the interfacial energy $\gamma_{\alpha\beta}$ in Eq. (3) should be corrected to $\hat{\gamma}_{\alpha\beta} = \gamma_{\alpha\beta}+\gamma_\alpha^c$. Since martensite transforms from austenite through quenching, the difference in the chemical energy density between austenite and martensite is so great that the energetic barrier only occurs when $\gamma_\alpha^c \gg \gamma_{\alpha\beta}$, as shown by Schoof et al. [84]. Therefore, for the 1D simulation of the martensitic phase transformation, it is necessary to set $\gamma_\alpha^c \gg \gamma_{\alpha\beta}$ to create an energetic barrier between the austenite and the martensite, even if there is no interfacial curvature.

In Eq. (6), ζ refers to the noise at the interface, which is expressed as:

$$\zeta = \begin{cases}\sum_{(\alpha,\beta>\alpha)}\phi_\alpha\phi_\beta\cdot A_\zeta & \left(t\ \%\ t_\zeta = 0\right)\\ 0 & \left(t\ \%\ t_\zeta \neq 0\right),\end{cases} \tag{9}$$

where A_ζ is the noise amplitude, % denotes the modulo operator, and t_ζ represents the time interval for the application of the noise. It should be noted that the constraint $\sum_\alpha^N \phi_\alpha = 1\ \ (0 \le \phi_\alpha \le 1)$ applies when there is noise at the interface. If the growth of a new phase is energetically favorable, autocatalytic nucleation occurs. Otherwise, the new phase will disappear after several time steps.

3. Dynamic mechanics in the multiphase-field model

For the mechanical model accounting for inertia effects, the governing equation for mechanical wave is presented in Section 3.1. Based on the evolution of martensite and the transformation strain, the increment of the stress and the elastic strain is derived in Section 3.2, and the velocity field is then obtained in Section 3.3. Considering the growth pattern of the martensitic variants, the formula for the mechanical fields is corrected in Section 3.4, by taking the direction of the mechanical wave propagation into account.

3.1. Governing equation

Supposing that $\boldsymbol{w} = \{w_1, w_2, w_3\}^\mathsf{T}$ denotes the displacement, ρ is the effective mass density [76], $\boldsymbol{\sigma}^m = \{\boldsymbol{\sigma}_1^m, \boldsymbol{\sigma}_2^m, \boldsymbol{\sigma}_3^m\}$ represents the stress tensor in the matrix notation, $\boldsymbol{x} = \{x_1, x_2, x_3\}^\mathsf{T}$ constructs the global Cartesian coordinate system, and $\boldsymbol{f} = \{f_1, f_2, f_3\}^\mathsf{T}$ describes the wave source, the wave equation is expressed as:

$$\frac{\partial^2\boldsymbol{w}}{\partial t^2} = \frac{1}{\rho}\left(\frac{\partial\boldsymbol{\sigma}_1^m}{\partial x_1} + \frac{\partial\boldsymbol{\sigma}_2^m}{\partial x_2} + \frac{\partial\boldsymbol{\sigma}_3^m}{\partial x_3}\right) + \boldsymbol{f}. \tag{10}$$

With $\boldsymbol{\sigma}$ as the stress tensor in the Voigt notation, $\bar{\boldsymbol{\varepsilon}}$ as the infinitesimal elastic strain tensor in the Voigt notation, and $\boldsymbol{K}$ as the 6×6 effective stiffness tensor [76], the constitutive equation reads:

$$\boldsymbol{\sigma} = \boldsymbol{K}\bar{\boldsymbol{\varepsilon}}. \tag{11}$$

Based on Eqs. (10) and (11), the governing equation for dynamic mechanics is expressed by $\boldsymbol{\sigma}$ and $\boldsymbol{v}$ as:

$$\frac{\partial\boldsymbol{u}}{\partial t} = \boldsymbol{C}_1\frac{\partial\boldsymbol{u}}{\partial x_1} + \boldsymbol{C}_2\frac{\partial\boldsymbol{u}}{\partial x_2} + \boldsymbol{C}_3\frac{\partial\boldsymbol{u}}{\partial x_3} + \boldsymbol{s}, \tag{12}$$

where $\boldsymbol{u} = \{\boldsymbol{\sigma}, \boldsymbol{v}\}^\mathsf{T}$ and $\boldsymbol{s}$ represents the wave source. $\boldsymbol{C}_1$, $\boldsymbol{C}_2$ and $\boldsymbol{C}_3$ are the coefficient matrices and can be found in the Appendix A.

The method used in the multiphase-field to solve Eq. (12) has been presented in detail in Liu et al. [76]. It should be pointed out that the displacement $\boldsymbol{w}$ and the velocity $\boldsymbol{v}$ correspond to the elastic deformation.

3.2. Derivation of stress and elastic strain

With the unit vectors $\{\boldsymbol{n}, \boldsymbol{s}, \boldsymbol{t}\} = \{\left(n_1, n_2, n_3\right)^\mathsf{T}, \left(s_1, s_2, s_3\right)^\mathsf{T}, \left(t_1, t_2, t_3\right)^\mathsf{T}\}$ constructing the local Cartesian coordinate system, and $\boldsymbol{n}$ as the vector normal to the diffuse interface, the stress tensor $\boldsymbol{\sigma}$ is transformed into the local coordinate system and divided into the normal components $\boldsymbol{\sigma}_n = \{\sigma_{nn}, \sigma_{nt}, \sigma_{ns}\}^\mathsf{T}$ and the tangential components $\boldsymbol{\sigma}_t = \{\sigma_{tt}, \sigma_{ss}, \sigma_{ts}\}^\mathsf{T}$, respectively. The same operation is applied to the elastic strain tensor $\bar{\boldsymbol{\varepsilon}}$, which results in the local elastic strain tensor with the normal components $\bar{\boldsymbol{\varepsilon}}_n = \{\bar{\varepsilon}_{nn}, \bar{\varepsilon}_{nt}, \bar{\varepsilon}_{ns}\}^\mathsf{T}$ and the tangential components $\bar{\boldsymbol{\varepsilon}}_t = \{\bar{\varepsilon}_{tt}, \bar{\varepsilon}_{ss}, \bar{\varepsilon}_{ts}\}^\mathsf{T}$. Correspondingly, for the phase/grain α, the local stiffness tensor $\boldsymbol{C}_B^\alpha$, which satisfies $\{\boldsymbol{\sigma}_n^\alpha, \boldsymbol{\sigma}_t^\alpha\}^\mathsf{T} = \boldsymbol{C}_B^\alpha\{\bar{\boldsymbol{\varepsilon}}_n^\alpha, \bar{\boldsymbol{\varepsilon}}_t^\alpha\}^\mathsf{T}$, is divided into four 3×3 submatrices:

$$\boldsymbol{C}_B^\alpha = \begin{pmatrix}\boldsymbol{C}_{nn}^\alpha & \boldsymbol{C}_{nt}^\alpha\\ \boldsymbol{C}_{tn}^\alpha & \boldsymbol{C}_{tt}^\alpha\end{pmatrix}. \tag{13}$$

Liu et al. [76] proved that the normal components $\boldsymbol{\sigma}_n$ and the tangential components $\bar{\boldsymbol{\varepsilon}}_t$ are continuous across the sharp interface. When considering the transformation strain $\tilde{\boldsymbol{\varepsilon}}$ on the basis of the derivation procedure in Liu et al. [76], it is easy to conclude that the tangential components $\boldsymbol{\epsilon}_t$ of the total strain $\boldsymbol{\varepsilon} = \bar{\boldsymbol{\varepsilon}} + \tilde{\boldsymbol{\varepsilon}}$ are continuous across the sharp interface. Therefore, the derivation procedure for the stress $\boldsymbol{\sigma}$ in Schneider et al. [72] can be adopted in this work, which results in:

$$\boldsymbol{\sigma} = \boldsymbol{K}\boldsymbol{\varepsilon} - \tilde{\boldsymbol{K}}\tilde{\boldsymbol{\chi}} = \boldsymbol{K}\boldsymbol{\varepsilon} + \boldsymbol{M}_\varepsilon^\mathsf{T}\begin{pmatrix}\overline{\boldsymbol{T}}_{nn}^{-1} & \mathbb{O}\\ \overline{\boldsymbol{T}}_{nt}^\mathsf{T}\overline{\boldsymbol{T}}_{nn}^{-1} & -\mathbb{I}\end{pmatrix}\begin{pmatrix}\tilde{\chi}_n\\ \tilde{\chi}_t\end{pmatrix}, \tag{14}$$

where $\tilde{\boldsymbol{K}}$ is defined as the analogous stiffness matrix corresponding to the transformation strain contribution $\tilde{\boldsymbol{\chi}} = \left(\tilde{\chi}_n, \tilde{\chi}_t\right)^\mathsf{T}$. $\mathbb{O}$ and $\mathbb{I}$ are the null matrix and the identity matrix, respectively. The transformation matrix $\boldsymbol{M}_\varepsilon$ is derived from $\{\boldsymbol{n}, \boldsymbol{s}, \boldsymbol{t}\}$ and is shown in the Appendix A. The matrices $\overline{\boldsymbol{T}}_{nn}$ and $\overline{\boldsymbol{T}}_{nt}$ are obtained from the local stiffness tensor $\boldsymbol{C}_B^\alpha$ and the interpolation function $h\left(\phi_\alpha\right)$ as:

$$\overline{\boldsymbol{T}}_{nn} = -\sum_\alpha\left(\boldsymbol{C}_{nn}^\alpha\right)^{-1}h\left(\phi_\alpha\right), \tag{15}$$

$$\overline{\boldsymbol{T}}_{nt} = \sum_\alpha\left(\boldsymbol{C}_{nn}^\alpha\right)^{-1}\boldsymbol{C}_{nt}^\alpha h\left(\phi_\alpha\right). \tag{16}$$

$\tilde{\chi}_n$ and $\tilde{\chi}_t$ are the transformation strain contribution in the normal direction and in the tangential direction, respectively, which are expressed as follows:

$$\tilde{\chi} = \begin{pmatrix}\tilde{\chi}_n\\ \tilde{\chi}_t\end{pmatrix} = \begin{pmatrix}\sum_\alpha\left[\tilde{\varepsilon}_n^\alpha + \left(\boldsymbol{C}_{nn}^\alpha\right)^{-1}\boldsymbol{C}_{nt}^\alpha\tilde{\varepsilon}_t^\alpha\right]h\left(\phi_\alpha\right)\\ \sum_\alpha\left[\boldsymbol{C}_{tt}^\alpha - \boldsymbol{C}_{tn}^\alpha\left(\boldsymbol{C}_{nn}^\alpha\right)^{-1}\boldsymbol{C}_{nt}^\alpha\right]\tilde{\varepsilon}_t^\alpha h\left(\phi_\alpha\right)\end{pmatrix} = \sum_\alpha\hat{\varepsilon}^\alpha h\left(\phi_\alpha\right), \tag{17}$$

where $\hat{\varepsilon}^\alpha = \left(\tilde{\varepsilon}_n^\alpha + \left(\boldsymbol{C}_{nn}^\alpha\right)^{-1}\boldsymbol{C}_{nt}^\alpha\tilde{\varepsilon}_t^\alpha, \left[\boldsymbol{C}_{tt}^\alpha - \boldsymbol{C}_{tn}^\alpha\left(\boldsymbol{C}_{nn}^\alpha\right)^{-1}\boldsymbol{C}_{nt}^\alpha\right]\tilde{\varepsilon}_t^\alpha\right)^\mathsf{T}$ is the analogous transformation strain for the phase/grain α.

Since martensite evolves at a high transformation rate, for each time step, it is assumed that the increment of the total strain induced by the phase transformation is zero, i.e., $\Delta\varepsilon\left(\Delta\boldsymbol{\phi}\right) = \Delta\bar{\boldsymbol{\varepsilon}}\left(\Delta\boldsymbol{\phi}\right) + \Delta\tilde{\boldsymbol{\varepsilon}}\left(\Delta\boldsymbol{\phi}\right) = \boldsymbol{0}$, where Δ represents the increment of the corresponding variable within the current time step. This means that $\Delta\bar{\boldsymbol{\varepsilon}}\left(\Delta\boldsymbol{\phi}\right) = -\Delta\tilde{\boldsymbol{\varepsilon}}\left(\Delta\boldsymbol{\phi}\right)$. Therefore, according to Eq. (14), the increment of the stress $\boldsymbol{\sigma}$ within the current time step is calculated as:

$$\Delta\boldsymbol{\sigma} = -\tilde{\boldsymbol{K}}\Delta\tilde{\boldsymbol{\chi}}. \tag{18}$$

Based on Eq. (17), the increment of the transformation strain contribution is:

$$\Delta\tilde{\boldsymbol{\chi}} = \sum_\alpha\hat{\varepsilon}^\alpha\Delta h\left(\phi_\alpha\right). \tag{19}$$

Since the sharp interface is replaced by the diffuse interface in the multiphase-field modeling, a proof of the equivalent increase of the transformation strain contribution is presented in Appendix B. $\Delta\boldsymbol{\sigma}$ is then inserted as the wave source into the total stress tensor $\boldsymbol{\sigma}$.

According to Eq. (11), the increment of the elastic strain tensor $\Delta\bar{\boldsymbol{\varepsilon}}$ is equivalent to:

$$\Delta\bar{\boldsymbol{\varepsilon}} = \boldsymbol{K}^{-1}\Delta\boldsymbol{\sigma}. \tag{20}$$

By referring to the derivation procedure of the effective stiffness matrix $\boldsymbol{K}$ in Liu et al. [76], Eq. (20) is rewritten as:

$$\Delta\bar{\boldsymbol{\varepsilon}} = M_{\varepsilon}^{-1}\begin{pmatrix} -\mathbb{I} & \overline{\boldsymbol{T}}_{nt}\overline{\boldsymbol{T}}_{tt}^{-1} \\ \mathbb{O} & -\overline{\boldsymbol{T}}_{tt}^{-1} \end{pmatrix}\Delta\tilde{\chi}, \tag{21}$$

where the matrix $\overline{\boldsymbol{T}}_{tt}$ is also derived from the local stiffness tensor $\boldsymbol{C}_B^{\alpha}$ and the interpolation function $h(\phi_{\alpha})$:

$$\overline{\boldsymbol{T}}_{tt} = \sum_{\alpha}\left(\boldsymbol{C}_{tt}^{\alpha} - \boldsymbol{C}_{tn}^{\alpha}\left(\boldsymbol{C}_{nn}^{\alpha}\right)^{-1}\boldsymbol{C}_{nt}^{\alpha}\right)h(\phi_{\alpha}). \tag{22}$$

3.3. Derivation of velocity

According to the definition of velocity, $\boldsymbol{v} = \{v_1, v_2, v_3\}^{\mathrm{T}} = \boldsymbol{w}/t$, it can be obtained that:

$$\Delta\boldsymbol{w} = \boldsymbol{v}\Delta t. \tag{23}$$

Since the displacement is induced by the transformation strain and $\Delta\bar{\boldsymbol{\varepsilon}}(\Delta\boldsymbol{\phi}) = -\Delta\tilde{\boldsymbol{\varepsilon}}(\Delta\boldsymbol{\phi})$, the elastic strain tensor in the matrix notation is expressed as $\bar{\varepsilon}_{ij}^{m} = -\frac{1}{2}\left(w_i/x_j + w_j/x_i\right)$ $(i,j=1,2,3)$. Similarly, the infinitesimal elastic rotation tensor is $\bar{\gamma}_{ij}^{m} = -\frac{1}{2}\left(w_i/x_j - w_j/x_i\right)$. Therefore, the following can be derived:

$$\Delta w_i = -\sum_{j=1}^{3}\left(\bar{\varepsilon}_{ij}^{m} + \bar{\gamma}_{ij}^{m}\right)\Delta x_{ji}, \tag{24}$$

where Δx_{ij} represents the movement of w_j in the direction of x_i. Therefore, based on Eqs. (23) and (24), it can be concluded that:

$$v_i = -\sum_{j=1}^{3}\left(\bar{\varepsilon}_{ij}^{m} + \bar{\gamma}_{ij}^{m}\right)V_{ij}, \tag{25}$$

where $V_{ij} = V_P$ $(i=j)$ and $V_{ij} = V_S$ $(i\neq j)$ respectively are the propagation velocities of the P-wave (primary wave or longitudinal wave) and the S-wave (secondary wave or transverse wave), which are calculated as:

$$V_P = \sqrt{\frac{K_{11}}{\rho}}, \tag{26}$$

$$V_S = \sqrt{\frac{K_{44}}{\rho}}. \tag{27}$$

During the martensitic phase transformation, it is assumed that the eigen-rotation tensor is equal to zero, i.e., $\tilde{\boldsymbol{\gamma}}^{m} = \boldsymbol{0}$. Hence, the correspondingly induced elastic rotation tensor is equal to zero, i.e., $\bar{\boldsymbol{\gamma}}^{m} = \boldsymbol{0}$. Thus, according to Eq. (25), the increase of the velocity $\boldsymbol{v}$ in the current time step is calculated as:

$$\Delta v_i = -\sum_{j=1}^{3}\Delta\bar{\varepsilon}_{ij}^{m}V_{ij}, \tag{28}$$

where the increment of the elastic strain tensor $\Delta\bar{\varepsilon}_{ij}^{m}$ can easily be obtained from Eq. (21). $\Delta\boldsymbol{v}$ is then inserted into the total velocity vector $\boldsymbol{v}$ as the wave source, similar to $\Delta\boldsymbol{\sigma}$.

3.4. Direction of mechanical wave propagation

A 2D example is shown in Fig. 1 to schematically discuss the direction of mechanical wave propagation caused by the transformation strain. An aqua-colored nucleus is predefined in the center of the domain. In order to simplify the analysis, the transformation strain of the aqua-colored phase is assumed as $(\tilde{\varepsilon}_{11}, 0, 0, 0, 0, 0)$, with $\tilde{\varepsilon}_{11} > 0$, and the Poisson's ratio $\nu = 0$. The nucleus grows into the fuchsia-colored area, as shown in Fig. 1(a). Figs. 1 (b) and (c) respectively show the increment of the stress $\Delta\sigma_{11}$ and the velocity Δv_1, calculated by Eqs. (18) and (28), where the colors blue and red denote negative and positive values, respectively. It is observed that Figs. 1 (a), (b) and (c) are incompatible. In Fig. 1(a), the grown nucleus compresses its surroundings in the direction x_1, which means that the left side of the nucleus should move to the left and the right side to the right. As for the top and bottom sides, they should stay there and not compress the surroundings, which is due to the symmetrical property and the Poisson's ratio $\nu = 0$. However, Figs. 1 (b) and (c) show that the entire fuchsia-colored area is compressed in the direction x_1 and moves to the right. This is not only inconsistent with the phase transformation in Fig. 1(a), but also non-physical.

It is worth analyzing the growth of the nucleus within the blue circle in Fig. 1(a), which is enlarged in Fig. 1(d). The nucleus develops a unit growth to the top right, with an angle θ to the direction x_1. It can be divided into a growth of $\cos\theta$ in the direction x_1 and $\sin\theta$ in the direction x_2. Therefore, the increment of the stress should be $\Delta\sigma_{11} = K_{11}\Delta\bar{\varepsilon}_{11}|n_1|$, and the increment of the velocity $\Delta v_1 = -V_P\Delta\bar{\varepsilon}_{11}n_1$, where $\Delta\bar{\varepsilon}_{11}$ is calculated from Eq. (21). The stress and velocity corrected by considering the direction of nucleus growth are shown in Figs. 1 (e) and (f). This means that the fuchsia area is compressed in the direction x_1 and moves outwards, but the amplitude decreases from the vertical center to the upper/lower area. This analysis procedure also applies to the other elements of the strain tensor, resulting in the following correction for the increase in stress and velocity:

$$(\Delta\boldsymbol{\sigma})^{c} = \boldsymbol{K}\left(\Delta\bar{\boldsymbol{\varepsilon}}\right)^{c}, \tag{29}$$

$$\Delta v_i^{c} = -\sum_{j=1}^{3}\left(\Delta\bar{\varepsilon}_{ij}^{m}\right)^{c}V_{ij}, \tag{30}$$

where the corrected elastic strain tensor in the matrix notation is calculated as:

$$\left(\Delta\bar{\varepsilon}_{ij}^{m}\right)^{c} = \bar{\varepsilon}_{ij}^{m}n_j. \tag{31}$$

Correspondingly, the corrected elastic strain tensor in the Voigt notation is:

$$\Delta\bar{\varepsilon}_{ij}^{c} = \begin{cases} \bar{\varepsilon}_{ii}^{m}|n_i| & (i=j) \\ \bar{\varepsilon}_{ij}^{m}|n_j| + \bar{\varepsilon}_{ji}^{m}|n_i| & (i<j). \end{cases} \tag{32}$$

The local time iteration in the mechanical model accounting for inertia effects and the global solver loop are provided in Appendix C.

4. Numerical simulation

The mechanical model accounting for inertia effects is validated in Section 4.1 using a 1D example, where the formation process of the martensitic morphology is analyzed along with the change in total mechanical energy, stress and velocity, as well as the velocity range for the transformation front. In Section 4.2, the model is applied to 2D simulations with one martensitic nucleus and multiple martensitic nuclei. For comparison, 2D modeling with static mechanics is also presented. It is concluded that the mechanical model accounting for inertia effects is more accurate for simulating the rapid displacive phase transformation.

4.1. 1D validation

A 1D example is shown in Fig. 2, where there are three different phases, i.e., the austenite (A), the first martensite variant (M_1) and the second martensite variant (M_2). The simulation setup and the material properties are shown in Tables 1 and 2. It should be pointed out that

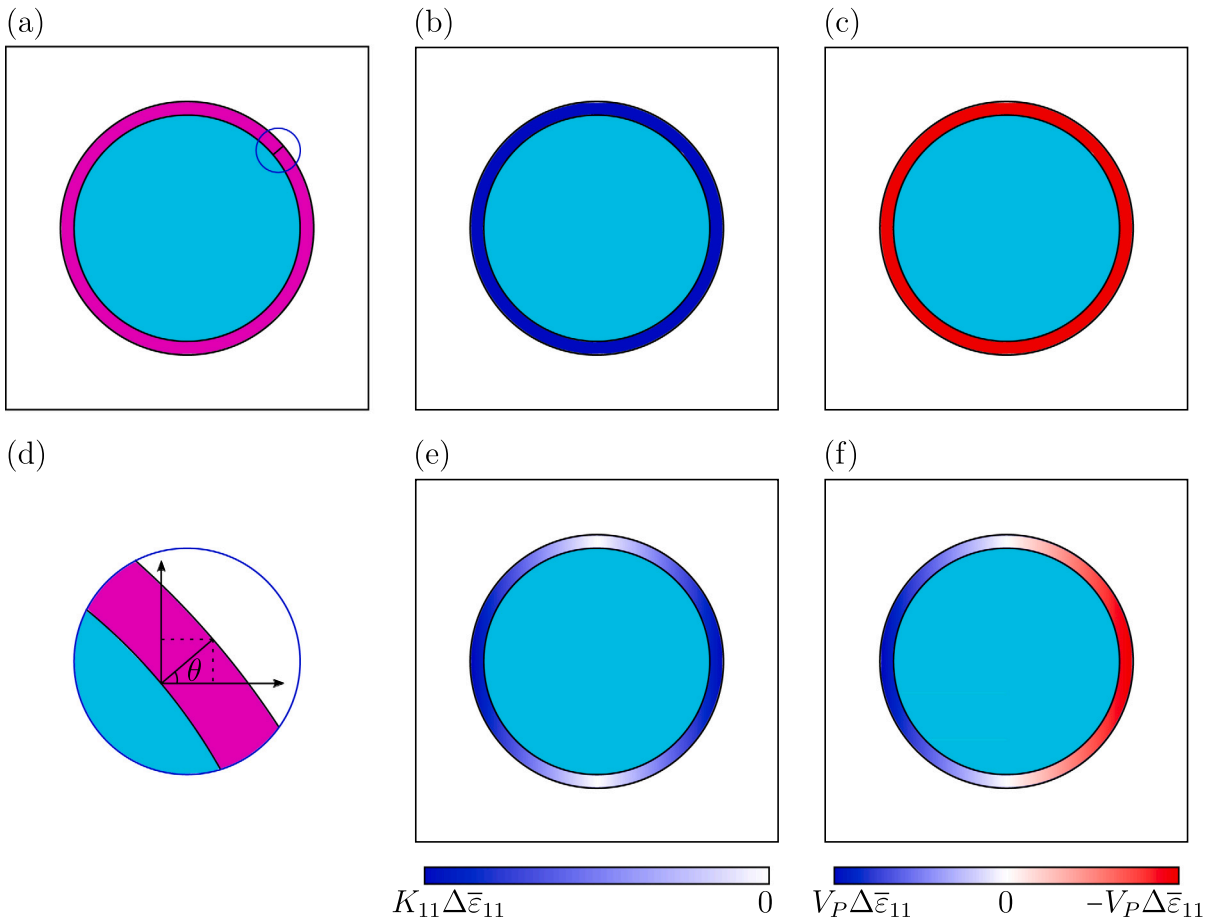

Fig. 1. Correction of the stress and the velocity, according to the growth of the nucleus. (a) The growth of the nucleus. (b) The stress and (c) the velocity fields calculated by Eqs. (18) and (28), which is not only inconsistent with the phase transformation in (a), but also non-physical. (d) Local analysis of the nucleus growth. (e) The corrected stress and (f) the corrected velocity fields based on the local analysis in (d).

Table 1
Simulation setup.

ϵ	A_ς	t_ς (ps)	Δt (ps)	τ_{AM}	$\tau_{M_1M_2}$	$\gamma_{\alpha\beta}$ (J/m^2)	γ_α^c (J/m^2)	Boundary
4	0.02	0.5	0.01	$0.00039/V_P$	∞	0.01	0.9	Non-reflective [76]

Table 2
Material properties.

Phase	ρ (kg/m^3)	E (GPa)	ν	f_{chem}^α (J/m^3)	$\tilde{\varepsilon}$
A				0	(0,0,0,0,0,0)
M_1	7800	200	0	-5.89×10^8	(0.03,0,0,0,0,0)
M_2				-5.89×10^8	(−0.03,0,0,0,0,0)

only 28.0% of the transformation strain is used to generate the kinetic energy that contributes to the driving force of the martensitic phase transformation, while the mechanical energy induced by the residual 72.0% of the transformation strain is to be consumed in other processes, such as plastic deformation. Unless explicitly stated, these parameters also apply to the 2D simulations in this section.

A martensitic nucleus M_1 is predefined in the parent austenite grain A, at the time $t = 0$ ps. At this time, there is no stress and no velocity. As the nucleus grows, the stress σ_{11} and the velocity v_1 propagate and accumulate, which are plotted in Fig. 2(b) in red and blue color, respectively, at the time $t = 5$ ps. Accordingly, the kinetic energy f_d increases, which counteracts the difference in chemical energy between austenite and martensite, until it is energetically favorable for a new M_2 to grow. When the new M_2 starts to grow, it releases the kinetic energy accumulated by the previous M_1, through reducing the absolute values of stress and velocity. As M_2 continues to grow, the absolute values of stress and velocity increase again, but with a different sign, as shown in Figs. 2 (a) and (b) at the time $t = 24$ ps. Then it becomes energetically favorable for a new M_1 to grow. This process repeats and causes the total kinetic energy to alternately increase and decrease, as well as the maximum absolute values of stress and velocity, as shown in Figs. 2 (c) and (d). According to Bekker et al. [85] and Amini et al. [86], there is only an elastic wave if the stress is below the critical value that triggers the stress-induced phase transformation. If the stress is greater than the critical value, but less than the plastic yield limit, both elastic wave and phase transformation occur. If the stress is above the plastic yield limit, the phase transformation is followed by plastic deformation.

In Fig. 2(b), it can be seen that there are evolving as well as fixed stresses and velocities. The evolving stress and velocity are at the front of the martensitic phase transformation. Their profiles and values change due to the transformation strain induced by the progressive martensitic phase transformation. Moreover, the fixed stress and velocity are overtaken by the front of the martensitic phase transformation. While propagating, their profiles and values are not affected by the martensitic phase transformation, except for those close to the transformation front, which is due to the fact that the velocity of the transformation front (VTF) is not exactly the same as the velocity of

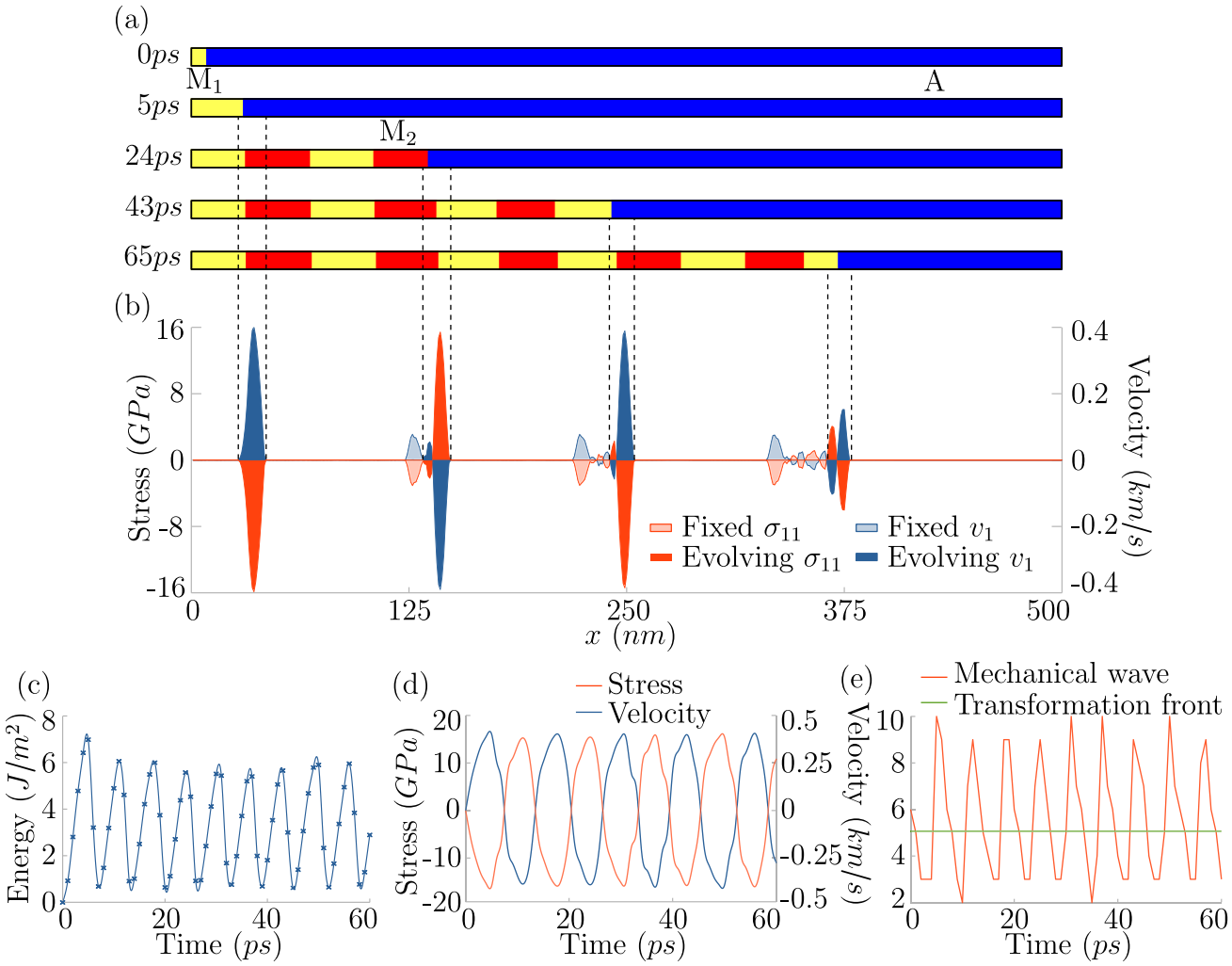

Fig. 2. 1D martensitic phase transformation. Evolution of (a) the martensitic variants and the corresponding (b) stress and velocity fields. Development of (c) the total kinetic energy and (d) the maximum/minimum values of stress and velocity in solid red and blue lines, respectively. (e) Velocities of the transformation front and the mechanical wave.

the mechanical wave (VMW), as shown in Fig. 2(e). The VMW is fixed at 5.06 km/s, according to Eq. (26), while the VTF fluctuates between 2 km/s and 10 km/s, with an average value of 5.49 km/s. This coincides with the phenomenon that the minimum total mechanical energy in Fig. 2(c) is greater than zero, except at $t = 0$ ps. In Fig. 2(b), the first fixed stress and velocity waves appear wider and higher than others, which is caused by the initial setting of the stress and velocity values. For the sake of simplicity, the initial stress and velocity in the simulation are set to zero, which should have approximately the profiles of the evolving stress and velocity at $t = 65$ ps. It can be seen that the following waves of the fixed stress and velocity are quite small.

In Fig. 2(e), the VTF decreases from $t = 0$ ps, since the driving force decreases due to the increment of the kinetic energy. When a new M_2 starts to grow, the VTF increases dramatically to around 10 km/s, since both the chemical energy and the kinetic energy contribute positively to the growth of the new M_2. The VTF then gradually decreases to around 2 km/s until a new M_1 occurs. This process repeats periodically and generates M_1 and M_2 variants alternately. The periodic variation of the VTF is also indicated by the change in the total kinetic energy in Fig. 2(c). It takes about 4 ps for the mechanical energy to increase from the minimum value to the maximum value, with the mechanical energy counteracting the chemical energy and reducing the driving force of the transformation, while the mechanical energy decreases by about 2 ps, with the mechanical energy having a positive effect on the nucleation and initial growth of a new martensite variant. In Amini et al. [86], it was reported that the VTF of the stress-induced phase transformation increases when the loading rate is increased.

4.2. 2D analysis

Two 2D examples are studied, i.e., with one M_1 nucleus at the center as shown in the first row and first column in Fig. 3, and with two M_1 and one M_2 nuclei at the boundary or corner as shown in the first row and fourth column in Fig. 3. For both cases, the simulation dimension is 500 nm × 500 nm. Compared to the 1D validation, $\tau_{AM} = 0.00036/V_P$, $\nu = 0.3$, and the respective transformation strains $\bar{\varepsilon}$ for the M_1 and M_2 variants are $(0.03, -0.03, 0, 0, 0, 0)$ and $(-0.03, 0.03, 0, 0, 0, 0)$. With the setting of the transformation strain $\bar{\varepsilon}$, a martensitic phase transformation without volumetric dilatation [84] is considered.

The simulation results are shown in Figs. 3 and 4. In Fig. 3, the first three columns correspond to the example with one M_1 nucleus. The last two columns correspond to the results from the second 2D example. The M_1 and M_2 variants are observed to nucleate alternately in the x_1 and x_2 directions, which is similar to the 1D case. Due to the restriction to 2D, both the M_1 and M_2 variants grow at an angle of 45° to the horizontal direction, which corresponds to the observation in Schoof et al. [84]. With the growth of martensite, the values of velocity and stress fluctuate between positive and negative. In the first three columns, the values of σ_{11} on the left and right have the same sign. It is the same for the values of σ_{22} at the bottom and top, while

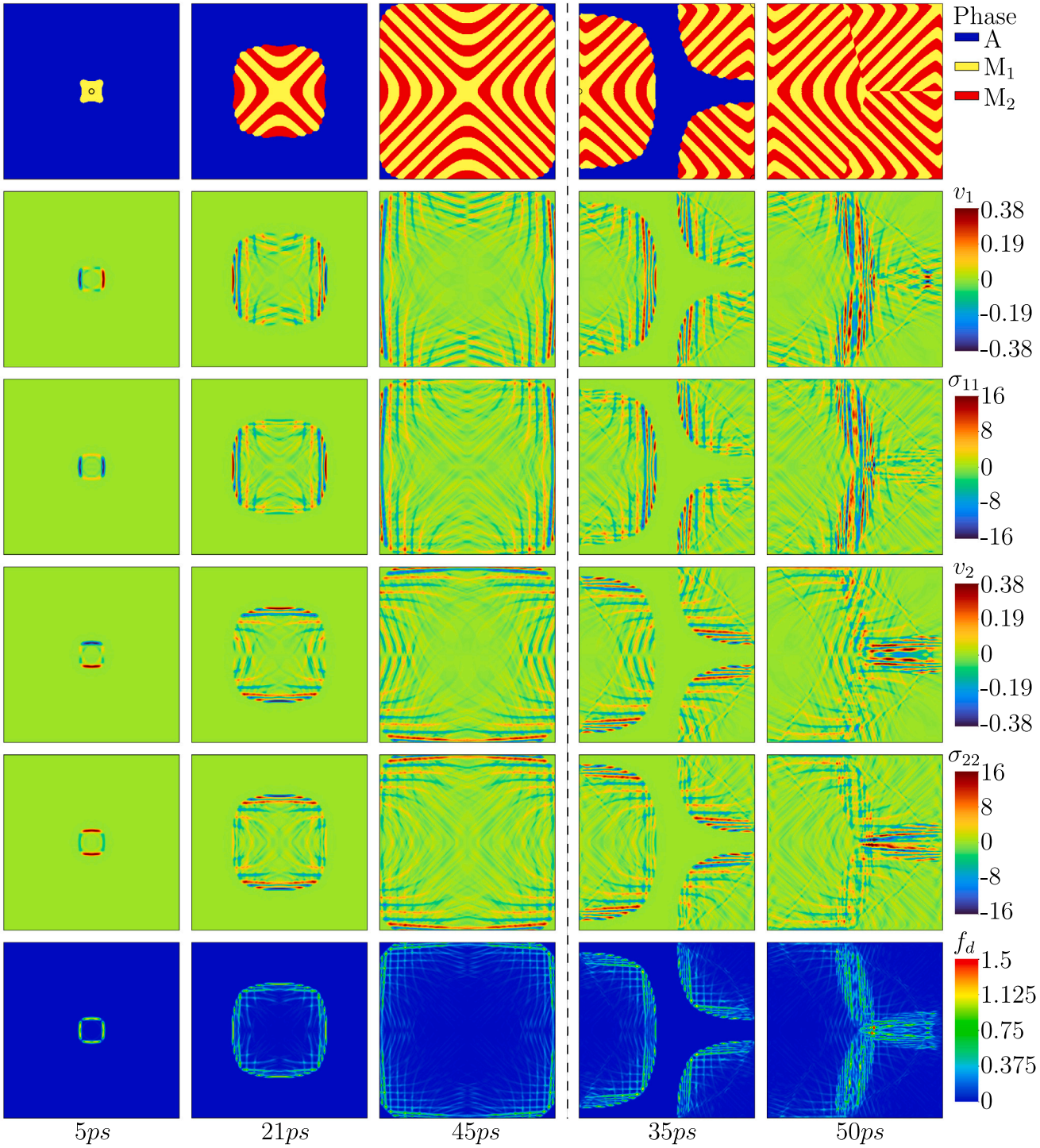

Fig. 3. 2D evolution of the martensitic variants, the velocity (km/s), the stress (GPa) and the mechanical energy (J/m^3) fields. The color legend for each row is at the right side, and the time for each column is at the bottom. In the first row and first column, the black circle at the center represents the initial M_1 nucleus. In the first row and fourth column, the black semicircle at the left boundary and the quarter circle at the upper-right corner are the initial M_1 nuclei, while the quarter circle at the lower-right corner is the initial M_2 nucleus.

they are opposite for the values of v_1 and v_2. This ensures that the martensite grows through a physical interaction with its environment, as analyzed in Section 3.4. In the last row, there is also some kinetic energy left from the transformation front, as the VTF does not exactly match the VMW, and the averaged VTF is slightly larger than the VMW, i.e., 6.03 km/s versus 5.31 km/s. This is similar to the observation in the 1D case. In the last two columns, the three nuclei start to grow at the boundary and stop when they meet. Meanwhile, the mechanical wave continues to propagate and overlap, causing the maximum kinetic energy density to reach 2.2×10^9 J/m^3 at $t = 50$ ps. It is much higher than the maximum kinetic energy density in the first four columns, which is $1.1 \sim 1.3 \times 10^9$ J/m^3.

The profile of ϕ_{M_1} over several cross-sections is plotted in Fig. 4. The value of ϕ_{M_1} smoothly shifts between 0 and 1, with a finite diffuse interface. There are some places where ϕ_{M_1} reaches neither 0 nor 1, such as in the middle of Figs. 4 (a) and (c), and at the side of Figs. 4

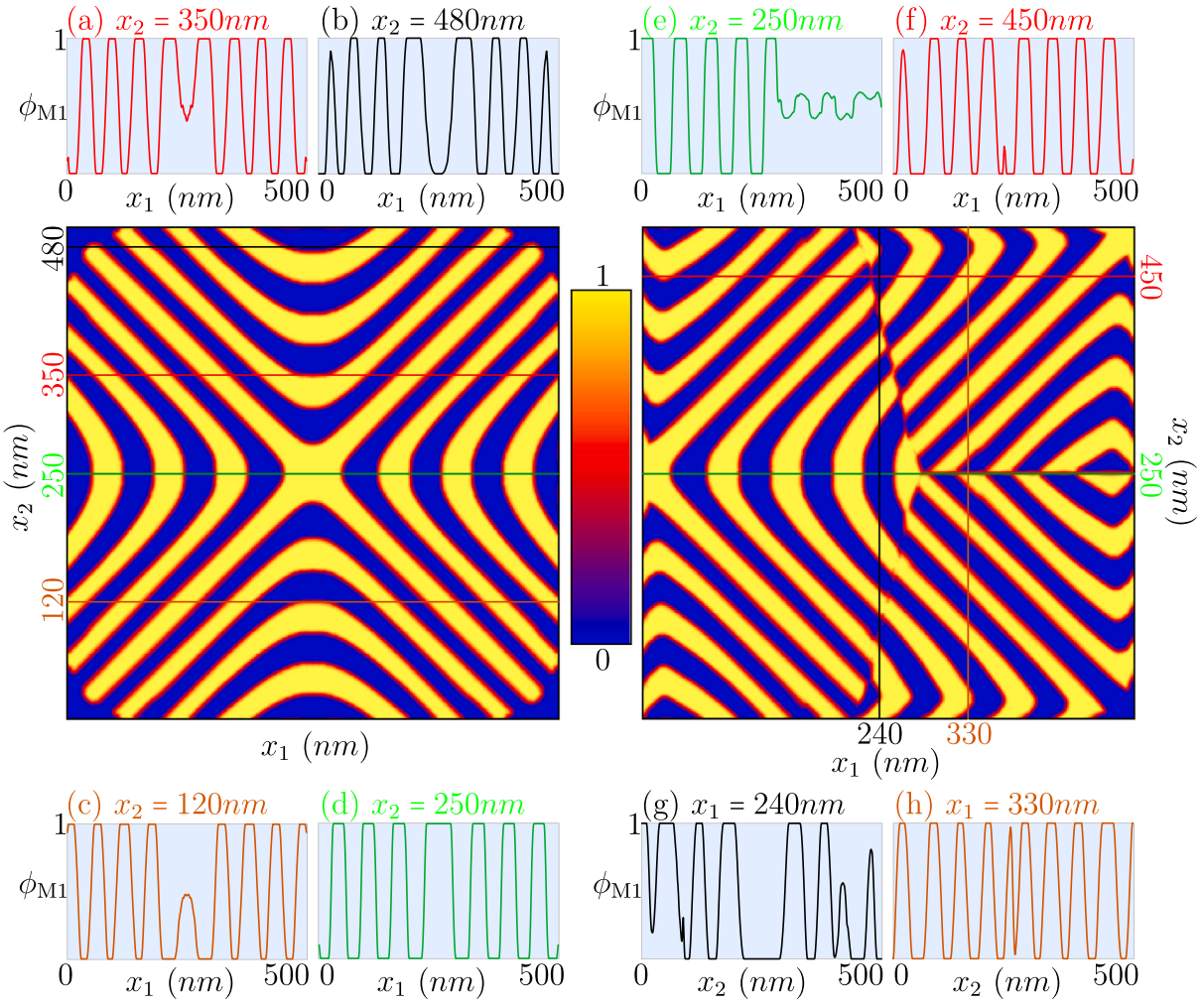

Fig. 4. Profile of ϕ_{M_1} at different cross-sections, where each profile corresponds to the cross-section with the same color. (a) to (d) for the first 2D example and (e) to (h) for the second 2D example.

(b), (f) and (g), because the cross-section is tangential to the diffuse interface. Compared to all interfaces in Fig. 4(d) and the left-sided interfaces in Fig. 4(e), the length of the diffuse interface appears slightly longer in other cross-sections, which is because these cross-sections are not perpendicular to the interfaces. On the right-hand side of Fig. 4(e), the value of ϕ_{M_1} fluctuates slightly around 0.5. This is because the growth from the upper corner M_1 meets that from the lower corner M_2 at $x_2 = 250$ nm, and both stop growing here. This phenomenon also leads to sharp jumps in ϕ_{M_1}, as shown in Figs. 4 (f), (g) and (h).

For the purpose of comparison, the 2D example with one M_1 nucleus at the center is also used to simulate martensitic phase transformation under static mechanics. In the static case, the displacement in the normal direction is fixed to zero, while it is free in the tangential direction. The transformation strains $\tilde{\varepsilon}$ for the M_1 and M_2 variants are changed to $(0.1, -0.1, 0, 0, 0, 0)$ and $(-0.1, 0.1, 0, 0, 0, 0)$, respectively. The noise amplitude A_ζ is reset to 0.1. The results at $t = 26$ ps and 45 ps are presented in Fig. 5.

Compared to the dynamic case, the absolute value of the non-zero transformation strain and the noise amplitude are larger, because the mechanical energy in the static case is distributed over the entire simulated domain in the equilibrium state and the dynamic effect is eliminated. The mechanical energy density around the transformation front decreases. Therefore, a higher percentage of the mechanical energy induced by the transformation strain and a higher noise amplitude are used to trigger nucleation and stimulate the growth of a new martensitic variant. On the other hand, the strongly utilized transformation strain, about 93.5%, restricts the width of the martensite, i.e., from about 32 nm to about 22 nm. Broader martensitic variants can be obtained with a smaller absolute value of the non-zero transformation strain. As a consequence, the VTF should also be reduced to produce a correct morphology of the martensite, which is not consistent with the intrinsic character of martensitic phase transformation, i.e., a rapid displacive phase transformation which is dominated by mechanical energy and which produces sound.

Even with the current settings, the averaged VTF in the static case is less than half of the VMW, i.e., 2.58 km/s compared to 5.31 km/s. In addition, it is much lower than that of the dynamic case, which is 6.03 km/s. This phenomenon can be observed from the results at $t = 45$ ps in Figs. 3 and 5. It is caused by the distribution pattern of the mechanical energy, as shown in the last row of Figs. 3 and 5. In the static case, the mechanical energy in the central horizontal/vertical line is in a state of equilibrium. This means that the difference in mechanical energy between the different phases is much smaller compared to the dynamic case. As a result, the static mechanical energy not only slows down the growth of the current martensitic variant, but also hardly contributes to the nucleation of a new martensitic variant. However, the stress concentration at the martensitic boundary generates a greater gradient of mechanical energy near the central horizontal/vertical line. Therefore, it is energetically favorable to introduce a new martensitic variant to reduce the mechanical energy gradient and stimulate the

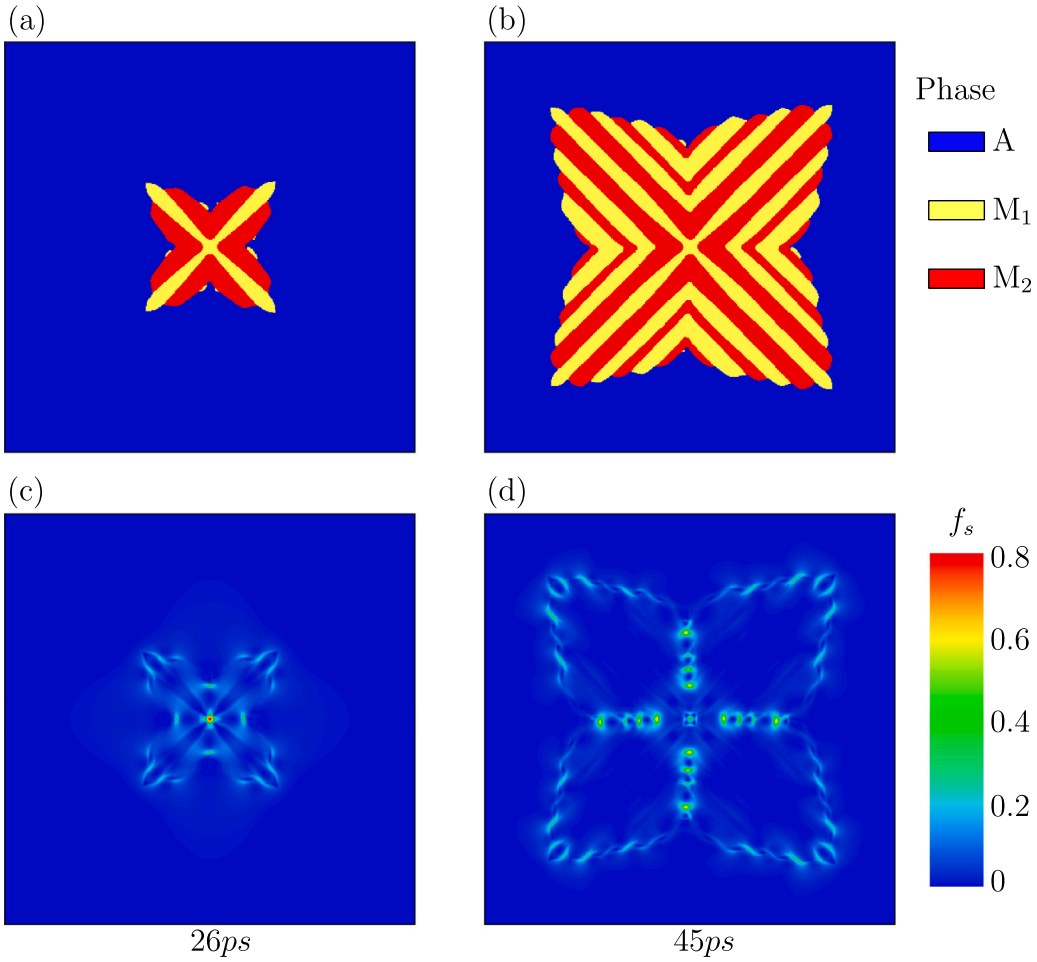

Fig. 5. Martensitic phase transformation with static mechanics. (a) and (b) are the evolution of the martensitic variants. (c) and (d) are the corresponding mechanical energy f_s (J/m^3).

phase transformation at these positions. This is confirmed by Figs. 5 (a) and (b), in which the nuclei appear at the boundary near the central horizontal/vertical line, rather than at the position of high interfacial curvature as in the dynamic case. Then the nuclei grow towards the central line and stop after they have met.

In summary, although the martensitic morphology is similar in the dynamic and static mechanical models, the martensitic variants nucleate and grow in different ways, due to the different mechanical phenomena. However, if the time scale is taken into account, the mechanical model accounting for inertia effects is more accurate in reproducing the process of the rapid displacive phase transformation.

5. Conclusions

In this paper, a mechanical model accounting for inertia effects is proposed to simulate and analyze the process of martensitic phase transformation.

In the simulation results, the martensitic variants are generated alternately. Since the mechanical model accounting for inertia effects is established based on the observation that martensitic phase transformation takes place close to the speed of sound, the VTF is compared with the VMW. When the driving force contributed by the kinetic energy plays a positive role in the growth of one martensitic variant, the VTF increases up to 10 km/s. While it decreases to 2 km/s, when the kinetic energy becomes energetically favorable to introduce another martensitic variant. As a result, the averaged VTF is slightly larger than the VMW. The direction of mechanical wave propagation is determined by the process of martensitic phase transformation, and in return strongly affects the morphology of martensite. With the signs of the stresses and velocities displayed in the 2D analysis, the formula for the mechanical fields derived in Section 3.4 is verified by the correct martensitic morphology. At different cross-sections, the profile of the phase state of M_1 is plotted to demonstrate the uniform shift of the corresponding order parameter ϕ_{M_1}. Due to the non-perpendicular angle between the cross-section and the diffuse interface or the encounter of different variants, ϕ_{M_1} does not reach 0/1 or jumps at some positions. The 2D results are also compared with those of static mechanics. Although the dynamic and static mechanical models produce a similar martensitic morphology, the martensitic variants nucleate and grow in different ways, due to different mechanical phenomena. In the dynamic case, nucleation occurs at the central horizontal/vertical line and grows at an angle of 45° to the horizontal direction, since the non-zero transformation strain is normal strain and the kinetic energy accumulates during propagation. While in the static case, nucleation starts near the central horizontal/vertical line and develops along the boundary of the adjacent martensitic variant, because of the stress concentration. From the time scale perspective, the mechanical model accounting for inertia effects is more accurate for simulating the rapid displacive phase transformation.

In this paper, a preliminary study on martensitic phase transformation, using the proposed mechanical model accounting for inertia effects, was presented. In the future, simulations considering other factors should be investigated, such as different Young's moduli and Poisson's ratios for different phases, different absolute values of non-zero

transformation strain in different directions, nucleation and growth of martensitic variants at the interface between two different austenitic grains, martensitic phase transformation in a 3D domain, and so forth.

CRediT authorship contribution statement

Xiaoying Liu: Writing – review & editing, Writing – original draft, Visualization, Validation, Software, Methodology, Investigation, Conceptualization. **Daniel Schneider:** Writing – review & editing, Supervision, Methodology, Investigation, Conceptualization. **Martin Reder:** Writing – review & editing, Software. **Paul W. Hoffrogge:** Writing – review & editing, Software. **Britta Nestler:** Writing – review & editing, Supervision, Resources, Funding acquisition.

Declaration of competing interest

The authors declare that they have no known competing financial interests or personal relationships that could have appeared to influence the work reported in this paper.

Data availability

Data will be made available on request.

Acknowledgments

These contributions to modeling were made at CELEST (Center for Electrochemical Energy Storage Ulm-Karlsruhe) and partially funded by the German Research Foundation (DFG), as part of the POLiS Cluster of Excellence (project ID 390874152). We would like to thank the Helmholtz Association, Germany for its support through the program "MSE No.: 43.31.01". This work was additionally funded by the German Federal Ministry of Education and Research (BMBF) with the project WirLeben SOFC (funding No.: 03SF0622D). The authors would like to thank Leon Geisen for his editorial support.

Appendix A. Coefficient matrices and transformation matrix

According to Eqs. (10) and (11), the coefficient matrices $\boldsymbol{C}_1$, $\boldsymbol{C}_2$ and $\boldsymbol{C}_3$ in Eq. (12) are expressed as:

$$\boldsymbol{C}_1 = \begin{pmatrix} 0 & 0 & 0 & 0 & 0 & 0 & K_{11} & 0 & 0 \\ 0 & 0 & 0 & 0 & 0 & 0 & K_{21} & 0 & 0 \\ 0 & 0 & 0 & 0 & 0 & 0 & K_{31} & 0 & 0 \\ 0 & 0 & 0 & 0 & 0 & 0 & 0 & 0 & 0 \\ 0 & 0 & 0 & 0 & 0 & 0 & 0 & 0 & K_{55} \\ 0 & 0 & 0 & 0 & 0 & 0 & 0 & K_{66} & 0 \\ \frac{1}{\rho} & 0 & 0 & 0 & 0 & 0 & 0 & 0 & 0 \\ 0 & 0 & 0 & 0 & 0 & \frac{1}{\rho} & 0 & 0 & 0 \\ 0 & 0 & 0 & 0 & \frac{1}{\rho} & 0 & 0 & 0 & 0 \end{pmatrix}, \tag{A.1}$$

$$\boldsymbol{C}_2 = \begin{pmatrix} 0 & 0 & 0 & 0 & 0 & 0 & 0 & K_{12} & 0 \\ 0 & 0 & 0 & 0 & 0 & 0 & 0 & K_{22} & 0 \\ 0 & 0 & 0 & 0 & 0 & 0 & 0 & K_{32} & 0 \\ 0 & 0 & 0 & 0 & 0 & 0 & 0 & 0 & K_{44} \\ 0 & 0 & 0 & 0 & 0 & 0 & 0 & 0 & 0 \\ 0 & 0 & 0 & 0 & 0 & 0 & K_{66} & 0 & 0 \\ 0 & 0 & 0 & 0 & 0 & \frac{1}{\rho} & 0 & 0 & 0 \\ 0 & \frac{1}{\rho} & 0 & 0 & 0 & 0 & 0 & 0 & 0 \\ 0 & 0 & 0 & \frac{1}{\rho} & 0 & 0 & 0 & 0 & 0 \end{pmatrix}, \tag{A.2}$$

$$\boldsymbol{C}_3 = \begin{pmatrix} 0 & 0 & 0 & 0 & 0 & 0 & 0 & 0 & K_{13} \\ 0 & 0 & 0 & 0 & 0 & 0 & 0 & 0 & K_{23} \\ 0 & 0 & 0 & 0 & 0 & 0 & 0 & 0 & K_{33} \\ 0 & 0 & 0 & 0 & 0 & 0 & 0 & K_{44} & 0 \\ 0 & 0 & 0 & 0 & 0 & 0 & K_{55} & 0 & 0 \\ 0 & 0 & 0 & 0 & 0 & 0 & 0 & 0 & 0 \\ 0 & 0 & 0 & 0 & \frac{1}{\rho} & 0 & 0 & 0 & 0 \\ 0 & 0 & 0 & \frac{1}{\rho} & 0 & 0 & 0 & 0 & 0 \\ 0 & 0 & \frac{1}{\rho} & 0 & 0 & 0 & 0 & 0 & 0 \end{pmatrix}. \tag{A.3}$$

The transformation matrix $\boldsymbol{M}_{\epsilon}$ in Eq. (14) is given by the unit vectors $\{\boldsymbol{n}, \boldsymbol{s}, \boldsymbol{t}\}$ as:

$$\boldsymbol{M}_{\epsilon} = \begin{pmatrix} n_1 n_1 & n_2 n_2 & n_3 n_3 & n_2 n_3 & n_1 n_3 & n_1 n_2 \\ 2 n_1 t_1 & 2 n_2 t_2 & 2 n_3 t_3 & n_2 t_3 + n_3 t_2 & n_1 t_3 + n_3 t_1 & n_1 t_2 + n_2 t_1 \\ 2 n_1 s_1 & 2 n_2 s_2 & 2 n_3 s_3 & n_2 s_3 + n_3 s_2 & n_1 s_3 + n_3 s_1 & n_1 s_2 + n_2 s_1 \\ s_1 s_1 & s_2 s_2 & s_3 s_3 & s_2 s_3 & s_1 s_3 & s_1 s_2 \\ t_1 t_1 & t_2 t_2 & t_3 t_3 & t_2 t_3 & t_1 t_3 & t_1 t_2 \\ 2 s_1 t_1 & 2 s_2 t_2 & 2 s_3 t_3 & s_2 t_3 + s_3 t_2 & s_1 t_3 + s_3 t_1 & s_1 t_2 + s_2 t_1 \end{pmatrix}. \tag{A.4}$$

Appendix B. Equivalent increment of transformation strain contribution

In order to prove the equivalent increment of the transformation strain contribution $\Delta\tilde{\chi}$, Fig. B.1 shows a 1D example to illustrate the proof procedure.

First, the case of the sharp interface in Fig. B.1(a) is analyzed. From Eq. (17), the transformation strain contribution from the phase/grain α is $\tilde{\chi}^{\alpha} = \hat{\epsilon}^{\alpha}$. When the sharp interface moves by Δx, the total increment of $\tilde{\chi}^{\alpha}$ becomes:

$$\Delta\tilde{X}^{\alpha}_{\text{sharp}} = \int_{x^s}^{x^e} \tilde{\chi}^{\alpha} \mathrm{d}x = \hat{\epsilon}^{\alpha} \Delta x, \tag{B.1}$$

where x^s and x^e are the position of the interface at the start and end of the movement Δx, respectively.

For the diffuse interface case in Fig. B.1(b), the transformation strain contribution from the phase/grain α is $\tilde{\chi}^{\alpha} = \hat{\epsilon}^{\alpha} h\left(\phi_{\alpha}\right)$. When the diffuse interface moves by Δx, the increment of the interpolation function $h\left(\phi_{\alpha}\right)$ is calculated as:

$$\Delta h\left(\phi_{\alpha}\right) = \begin{cases} 0 & \left(x \le x_1\right) \\ 1 - h_s\left(\phi_{\alpha}\right) & \left(x_1 < x \le x_1 + \Delta x\right) \\ h_e\left(\phi_{\alpha}\right) - h_s\left(\phi_{\alpha}\right) & \left(x_1 + \Delta x < x \le x_2\right) \\ h_e\left(\phi_{\alpha}\right) & \left(x_2 < x < x_2 + \Delta x\right) \\ 0 & \left(x \ge x_2 + \Delta x\right), \end{cases} \tag{B.2}$$

where $h_s\left(\phi_{\alpha}\right)$ and $h_e\left(\phi_{\alpha}\right)$ are the respective interpolation functions at the beginning and end of the interface movement Δx, while x_1 and x_2 are the beginning and end of the diffuse interface with the interpolation function $h_s\left(\phi_{\alpha}\right)$. Supposing that $H\left(\phi_{\alpha}\right)$ is the antiderivative of the interpolation function $h\left(\phi_{\alpha}\right)$, the total increment of $\tilde{\chi}^{\alpha}$ is then calculated as:

$$\Delta\tilde{X}^{\alpha}_{\text{diffuse}} = \int_{x_1}^{x_2+\Delta x} \hat{\epsilon}^{\alpha} \Delta h\left(\phi_{\alpha}\right) \mathrm{d}x = \hat{\epsilon}^{\alpha} \left(\Delta x + H_e\left(\phi_{\alpha}\right)|_{x_1+\Delta x}^{x_2+\Delta x} - H_s\left(\phi_{\alpha}\right)|_{x_1}^{x_2}\right). \tag{B.3}$$

From Fig. B.1, it is easy to conclude that $H_e\left(\phi_{\alpha}\right)|_{x_1+\Delta x}^{x_2+\Delta x} = H_s\left(\phi_{\alpha}\right)|_{x_1}^{x_2}$. Therefore, Eq. (B.4) is equal to:

$$\Delta\tilde{X}^{\alpha}_{\text{diffuse}} = \hat{\epsilon}^{\alpha} \Delta x. \tag{B.4}$$

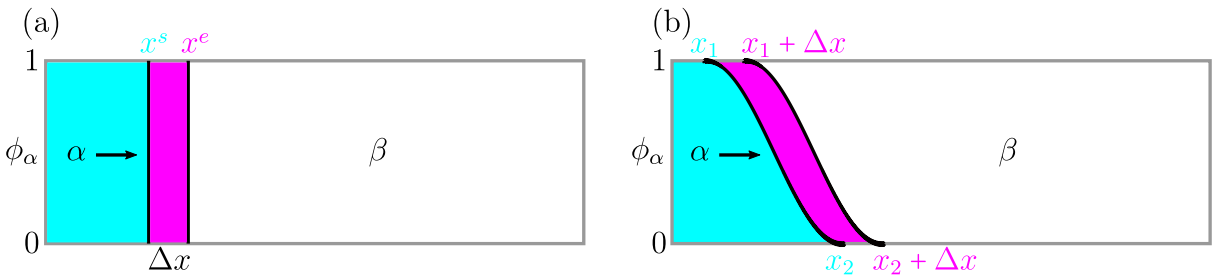

Fig. B.1. Propagation of the interface. (a) and (b) respectively are the sharp and diffuse interface cases.

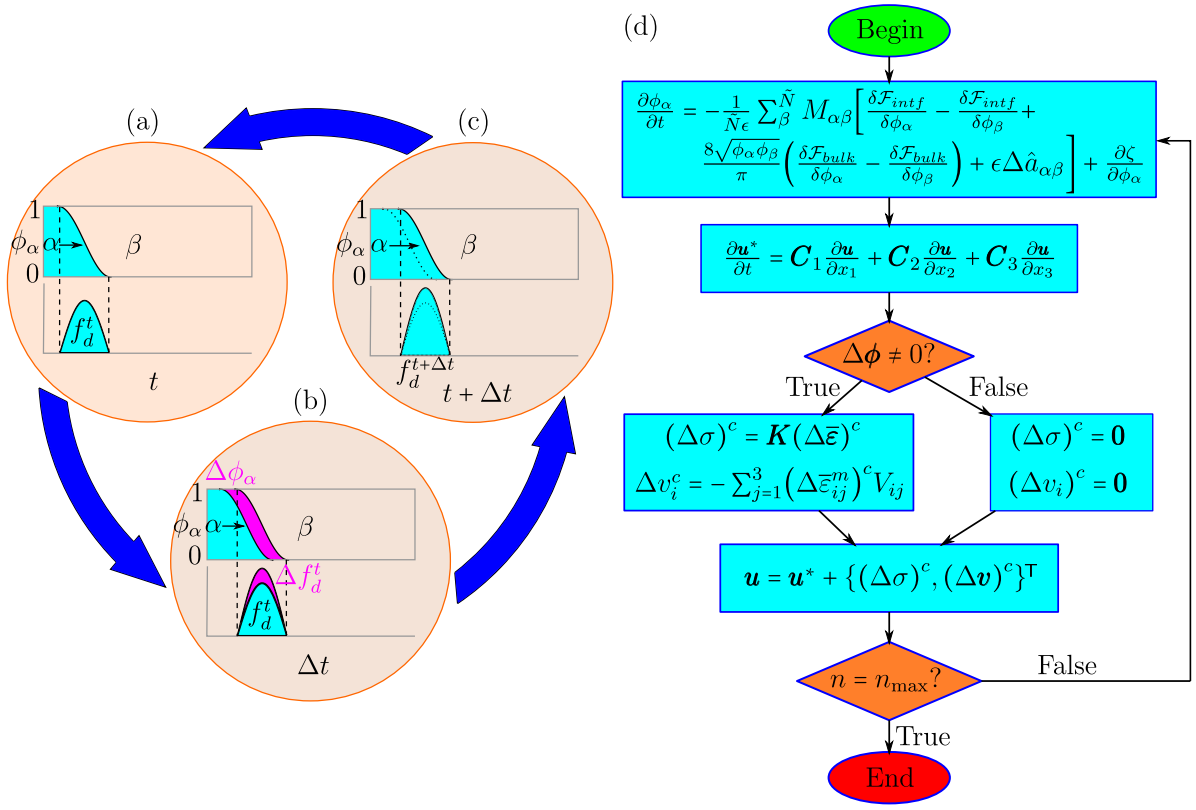

Fig. C.1. Numerical scheme for simulation. (a) to (c) are the local time iteration in the mechanical model accounting for inertia effects. (d) Global solver loop.

From Eqs. (B.1) and (B.4), it can be concluded that the increment of the transformation strain contribution is equivalent in the case of the sharp interface and in the case of the diffuse interface.

Appendix C. Local time iteration in mechanical model accounting for inertia effects and global solver loop

The implementation of dynamic mechanics is described as shown in Figs. C.1 (a)–(c), where a 1D case is illustrated as an example. In each time step, the kinetic energy density f_d^t is plotted according to the current state of the order parameters, as shown in Fig. C.1(a). In the following time interval Δt, the order parameters evolve under the driving force, which comes from the interfacial energy, the chemical energy and the kinetic energy, as shown in Fig. C.1(b). The kinetic energy density f_d^t then propagates under the updated state of the order parameters. Assuming that the increment of the order parameters is $\Delta\boldsymbol{\phi}$, the increment of the kinetic energy density Δf_d^t is calculated and added to the total kinetic energy density f_d^t, resulting in the updated kinetic energy density $f_d^{t+\Delta t}$. Therefore, at the end of the current time step as shown in Fig. C.1(c), both the order parameters and the kinetic energy density are updated, which form the initial state of the next time step.

Based on the derivations in Sections 2 and 3, the solver loop for the multiphase-field model is demonstrated in Fig. C.1(d). The program begins by solving the evolution equation for each order parameter, i.e., Eq. (6). A numerical solution of the governing equation for the mechanical wave follows, i.e., Eq. (12), but without considering the source term $\boldsymbol{s}$. This means that the mechanical wave propagates over the domain with the updated order parameters. Then $\Delta\boldsymbol{\phi}$ is calculated by comparing the values in the current time step with those in the previous time step to determine whether a wave source is present or not. More precisely, if $\Delta\boldsymbol{\phi} \neq \boldsymbol{0}$, the increments of the stress tensor $\Delta\boldsymbol{\sigma}$ and the velocity vector $\Delta\boldsymbol{v}$ are calculated according to Eqs. , respectively. Otherwise, both increments are set to $\boldsymbol{0}$. Then the mechanical fields are updated by adding the propagated and the increased stress and velocity fields. Finally, the number of calculated loops n is compared with the predefined number of loops $n_{\max}$ to determine whether the solver loop continues to run or not.

References

[1] Fischer T, Zhou T, Dahlberg CF, Hedström P. Relating stress/strain heterogeneity to lath martensite strength by experiments and dislocation density-based crystal plasticity. Int J Plast 2024;103917.

[2] Liu H, Shang X, He B, Liang Z. Strain rate dependence of strengthening mechanisms in ultrahigh strength lath martensite. Int J Plast 2023;161:103495.
[3] Kwak K, Mine Y, Morito S, Ohmura T, Takashima K. Correlation between strength and hardness for substructures of lath martensite in low-and medium-carbon steels. Mater Sci Eng A 2022;856:144007.
[4] Zhao Y, Liu W, Zhang T, Sun Z, Wang Y, Fan Y, Dong B. Assessment of the correlation between $M_{23}C_6$ precipitates and pitting corrosion resistance of 0Cr13 martensitic stainless steel. Corros Sci 2021;189:109580.
[5] Zhao Y, Liu W, Fan Y, Zhang T, Dong B, Chen L, Wang Y. Influence of microstructure on the corrosion behavior of super 13Cr martensitic stainless steel under heat treatment. Mater Charact 2021;175:111066.
[6] Miao Y, Vlassak JJ. Explosive martensitic transformation of supercooled austenite in CuZr-based thin-film shape memory alloys. Acta Mater 2020;200:162–70.
[7] Liu T, Liang L, Raabe D, Dai L. The martensitic transition pathway in steel. J. Mater. Sci. Technol. 2023;134:244–53.
[8] Liang L, Tong W, Xu J, Wang X, Wang X, Zhao Y, Wang W, Wang H, Tian J, Tian Q, et al. Evidence for austenite to non-modulated martensite transformation crystallography and variant organization in Ni-Mn-Ga-Co ferromagnetic shape memory alloys. Acta Mater 2023;254:119022.
[9] Clapp P. How would we recognize a martensitic transformation if it bumped into us on a dark & austy night? In: Journal de Physique IV Proceedings. 1995, p. C8–11.
[10] Xiao R, Hou B, Sun Q, Zhao H, Li Y. An experimental investigation of the nucleation and the propagation of NiTi martensitic transformation front under impact loading. Int J Impact Eng 2020;140:103559.
[11] Planes A, Mañosa L, Vives E. Acoustic emission in martensitic transformations. J Alloys Compd 2013;577:S699–704.
[12] Schwabe S, Lünser K, Schmidt D, Nielsch K, Gaal P, Fähler S. What is the speed limit of martensitic transformations? Sci. Technol. Adv. Mater. 2022;23(1):633–41.
[13] Kashchenko M, Chashchina V, Vikharev S. Dynamic model of the formation of twinned martensite crystals: I. Control wave process and the removal of degeneracy in twin-boundary orientation. Phys. Metals Metallogr. 2010;110(3):200–9.
[14] Kashchenko M, Chashchina V, Vikharev S. Dynamic model of the formation of twinned martensite crystals: II. Pretransition states and relationships between the volumes of the twin components. Phys. Metals Metallogr. 2010;110(4):305–17.
[15] Reddy KV, Deng C, Pal S. Dynamic characterization of shock response in crystalline-metallic glass nanolaminates. Acta Mater 2019;164:347–61.
[16] Konnur T, Reddy KV, Pal S. Effect of variation in inclination angle of $\sum 5$ tilt grain boundary on the shock response of Ni bicrystals. Appl Phys A 2021;127:1–18.
[17] Wei Z, Ma X, Ke C, Zhang X. Distinct migration mechanisms of stepped FCC/BCC martensitic interfaces associated with typical orientation relationships: a molecular dynamics study. J Mater Sci 2022;57(42):19857–71.
[18] Dean A, Kumar PAV, Reinoso J, Gerendt C, Paggi M, Mahdi E, Rolfes R. A multi phase-field fracture model for long fiber reinforced composites based on the puck theory of failure. Compos Struct 2020;251:112446.
[19] Cui C, Ma R, Martínez-Pañeda E. A generalised, multi-phase-field theory for dissolution-driven stress corrosion cracking and hydrogen embrittlement. J Mech Phys Solids 2022;166:104951.
[20] Kunwar A, Hektor J, Nomoto S, Coutinho YA, Moelans N. Combining multi-phase field simulation with neural network analysis to unravel thermomigration accelerated growth behavior of Cu_6Sn_5 IMC at cold side Cu–Sn interface. Int J Mech Sci 2020;184:105843.
[21] Chen L-Q. Phase-field models for microstructure evolution. Annu Rev Mater Sci 2002;32(1):113–40.
[22] Boettinger WJ, Warren JA, Beckermann C, Karma A. Phase-field simulation of solidification. Annu Rev Mater Sci 2002;32(1):163–94.
[23] Moelans N, Blanpain B, Wollants P. An introduction to phase-field modeling of microstructure evolution. CALPHAD 2008;32(2):268–94.
[24] Echebarria B, Folch R, Karma A, Plapp M. Quantitative phase-field model of alloy solidification. Phys Rev E 2004;70(6):061604.
[25] Ode M, Kim SG, Suzuki T. Recent advances in the phase-field model for solidification. ISIJ Int. 2001;41(10):1076–82.
[26] Gránásy L, Pusztai T, Warren JA. Modelling polycrystalline solidification using phase field theory. J Phys: Condens Matter 2004;16(41):R1205.
[27] Jacqmin D. Calculation of two-phase Navier–Stokes flows using phase-field modeling. J Comput Phys 1999;155(1):96–127.
[28] Lamorgese AG, Molin D, Mauri R. Phase field approach to multiphase flow modeling. Milan J Math 2011;79:597–642.
[29] Lin Y, Skjetne P, Carlson A. A phase field model for multiphase electro-hydrodynamic flow. Int J Multiph Flow 2012;45:1–11.
[30] Simoes M, Martinez-Paneda E. Phase field modelling of fracture and fatigue in Shape Memory Alloys. Comput Methods Appl Mech Engrg 2021;373:113504.
[31] Borden MJ, Verhoosel CV, Scott MA, Hughes TJ, Landis CM. A phase-field description of dynamic brittle fracture. Comput Methods Appl Mech Engrg 2012;217:77–95.
[32] Kuhn C, Müller R. A continuum phase field model for fracture. Eng Fract Mech 2010;77(18):3625–34.
[33] Nguyen-Thanh N, Li W, Huang J, Zhou K. Multi phase-field modeling of anisotropic crack propagation in 3D fiber-reinforced composites based on an adaptive isogeometric meshfree collocation method. Comput Methods Appl Mech Engrg 2022;393:114794.
[34] Singh A, Pal S. Multi-phase field modeling for various fracture mechanisms in composites. Eng Fract Mech 2021;241:107348.
[35] Kumar PAV, Dean A, Reinoso J, Paggi M. A multi phase-field-cohesive zone model for laminated composites: Application to delamination migration. Compos. struct. 2021;276:114471.
[36] Daubner S, Dillenz M, Pfeiffer LF, Gauckler C, Rosin M, Burgard N, Martin J, Axmann P, Sotoudeh M, Groß A, et al. Combined study of phase transitions in the P2-type $Na_XNi_{1/3}Mn_{2/3}O_2$ cathode material: experimental, ab-initio and multiphase-field results. npj Comput. Mater. 2024;10(1):75.
[37] Ombrini P, Bazant MZ, Wagemaker M, Vasileiadis A. Thermodynamics of multi-sublattice battery active materials: from an extended regular solution theory to a phase-field model of $LiMn_yFe_{1-y}PO_4$. npj Comput. Mater. 2023;9(1):148.
[38] L'vov PE, Tikhonchev MY, Sibatov RT. Phase-field model of ion transport and intercalation in lithium-ion battery. J Energy Storage 2022;50:104319.
[39] Basak A, Levitas VI. A multiphase phase-field study of three-dimensional martensitic twinned microstructures at large strains. Contin Mech Thermodyn 2023;35(4):1595–624.
[40] Tuma K, Rezaee-Hajidehi M, Hron J, Farrell P, Stupkiewicz S. Phase-field modeling of multivariant martensitic transformation at finite-strain: computational aspects and large-scale finite-element simulations. Comput Methods Appl Mech Engrg 2021;377:113705.
[41] Babaei H, Levitas VI. Finite-strain scale-free phase-field approach to multivariant martensitic phase transformations with stress-dependent effective thresholds. J Mech Phys Solids 2020;144:104114.
[42] Levitas VI. Thermodynamically consistent phase field approach to phase transformations with interface stresses. Acta Mater 2013;61(12):4305–19.
[43] Javanbakht M, Barati E. Martensitic phase transformations in shape memory alloy: phase field modeling with surface tension effect. Comput Mater Sci 2016;115:137–44.
[44] Levitas VI, Javanbakht M. Surface tension and energy in multivariant martensitic transformations: phase-field theory, simulations, and model of coherent interface. Phys Rev Lett 2010;105(16):165701.
[45] Xu B, Kang G. Phase field simulation on the super-elasticity, elastocaloric and shape memory effect of geometrically graded nano-polycrystalline NiTi shape memory alloys. Int J Mech Sci 2021;201:106462.
[46] Xu T, Wang C, Zhu Y, Wang Y, Yan Y, Wang J, Shimada T, Kitamura T. Efficient phase-field simulation for linear superelastic NiTi alloys under temperature gradients. Int J Mech Sci 2023;259:108592.
[47] Ahluwalia R, Mikula J, Laskowski R, Quek SS. Phase field simulation of martensitic-transformation-induced plasticity in steel. Phys Rev Mater 2020;4(10):103607.
[48] Zhang X, Shen G, Xu J, Gu J. Analysis of martensitic transformation plasticity under various loadings in a low-carbon steel: an elastoplastic phase field study. Metall Mater Trans A 2020;51:4853–67.
[49] Mo H, Liu G, Mao Y, Shen Y, Wang J. Dual-interface model for twinning in the coupled crystal plasticity finite element–phase field method. Int J Plast 2022;158:103441.
[50] Xie X, Kang G, Kan Q, Yu C. Phase-field theory based finite element simulation on thermo-mechanical cyclic deformation of polycrystalline super-elastic NiTi shape memory alloy. Comput Mater Sci 2020;184:109899.
[51] Li X, Su Y. A phase-field study of the martensitic detwinning in NiTi shape memory alloys under tension or compression. Acta Mech 2020;231(4):1539–57.
[52] Xi S, Su Y. Phase field study of the microstructural dynamic evolution and mechanical response of NiTi shape memory alloy under mechanical loading. Materials 2021;14(1):183.
[53] Cui S, Wan J, Zuo X, Chen N, Zhang J, Rong Y. Three-dimensional, non-isothermal phase-field modeling of thermally and stress-induced martensitic transformations in shape memory alloys. Int J Solids Struct 2017;109:1–11.
[54] Wang D, Liang Q, Zhao S, Zhao P, Zhang T, Cui L, Wang Y. Phase field simulation of martensitic transformation in pre-strained nanocomposite shape memory alloys. Acta Mater 2019;164:99–109.
[55] Ohmer D, Yi M, Gutfleisch O, Xu B-X. Phase-field modelling of paramagnetic austenite–ferromagnetic martensite transformation coupled with mechanics and micromagnetics. Int J Solids Struct 2022;238:111365.
[56] Lázpita P, L'vov V, Fernández JR, Barandiarán J, Chernenko V. Combined effect of magnetic field and hydrostatic pressure on the phase transitions exhibited by Ni-Mn-In metamagnetic shape memory alloy. Acta Mater 2020;193:1–9.
[57] Lázpita P, Pérez-Checa A, Barandiarán JM, Ammerlaan A, Zeitler U, Chernenko V. Suppression of martensitic transformation in Ni-Mn-In metamagnetic shape memory alloy under very strong magnetic field. J Alloys Compd 2021;874:159814.
[58] Jafarzadeh H, Levitas VI, Farrahi GH, Javanbakht M. Phase field approach for nanoscale interactions between crack propagation and phase transformation. Nanoscale 2019;11(46):22243–7.

[59] Amirian B, Jafarzadeh H, Abali BE, Reali A, Hogan JD. Thermodynamically-consistent derivation and computation of twinning and fracture in brittle materials by means of phase-field approaches in the finite element method. Int J Solids Struct 2022;252:111789.
[60] Cui S, Cui Y, Wan J, Rong Y, Zhang J. Grain size dependence of the martensite morphology–A phase-field study. Comput Mater Sci 2016;121:131–42.
[61] Rezaee-Hajidehi M, Stupkiewicz S. Phase-field modeling of multivariant martensitic microstructures and size effects in nano-indentation. Mech Mater 2020;141:103267.
[62] Cho J-Y, Idesman A, Levitas V, Park T. Finite element simulations of dynamics of multivariant martensitic phase transitions based on Ginzburg–Landau theory. Int J Solids Struct 2012;49(14):1973–92.
[63] Idesman AV, Cho J-Y, Levitas VI. Finite element modeling of dynamics of martensitic phase transitions. Appl Phys Lett 2008;93(4).
[64] Schmidt SD, Ammar K, Dornisch W, Forest S, Müller R. Phase field model for the martensitic transformation: comparison of the Voigt/Taylor and Khachaturyan approach. Contin Mech Thermodyn 2021;33:2075–94.
[65] Chatterjee S, Schwen D, Moelans N. A computationally efficient and mechanically compatible multi-phase-field model applied to coherently stressed three-phase solids. Comput Mater Sci 2023;218:111969.
[66] Von Oertzen V, Kiefer B. Unequally and non-linearly weighted averaging operators as a general homogenization approach for phase field modeling of phase transforming materials. Shape Mem. Superelasticity 2022;8(4):425–37.
[67] Yang Y, Fathidoost M, Oyedeji TD, Bondi P, Zhou X, Egger H, Xu B-X. A diffuse-interface model of anisotropic interface thermal conductivity and its application in thermal homogenization of composites. Scr Mater 2022;212:114537.
[68] Salama H, Ali MA, Shchyglo O, Steinbach I. Phase-field simulation framework for modeling martensite and bainite formation in steel. Comput Mater Sci 2024;241:113033.
[69] Shchyglo O, Ali MA, Salama H. Efficient finite strain elasticity solver for phase-field simulations. npj Comput. Mater. 2024;10(1):52.
[70] Böttger B, Apel M, Budnitzki M, Eiken J, Laschet G, Zhou B. Calphad coupled phase-field model with mechano-chemical contributions and its application to rafting of γ' in CMSX-4. Comput Mater Sci 2020;184:109909.
[71] Durga A, Wollants P, Moelans N. Evaluation of interfacial excess contributions in different phase-field models for elastically inhomogeneous systems. Modelling Simul. Mater. Sci. Eng. 2013;21(5):055018.
[72] Schneider D, Tschukin O, Choudhury A, Selzer M, Böhlke T, Nestler B. Phase-field elasticity model based on mechanical jump conditions. Comput Mech 2015;55(5):887–901.
[73] Schöller L, Schneider D, Prahs A, Nestler B. Phase-field modeling of crack propagation based on multi-crack order parameters considering mechanical jump conditions. PAMM 2023;22(1):e202200039.
[74] Herrmann C, Schneider D, Schoof E, Schwab F, Nestler B. Phase-field model for the simulation of brittle-anisotropic and ductile crack propagation in composite materials. Materials 2021;14(17):4956.
[75] Herrmann C, Schoof E, Schneider D, Schwab F, Reiter A, Selzer M, Nestler B. Multiphase-field model of small strain elasto-plasticity according to the mechanical jump conditions. Comput Mech 2018;62:1399–412.
[76] Liu X, Schneider D, Daubner S, Nestler B. Simulating mechanical wave propagation within the framework of phase-field modelling. Comput Methods Appl Mech Engrg 2021;381:113842.
[77] Liu X, Schneider D, Nestler B. Phase-field modelling of mechanical wave propagation in polycrystalline materials: Validation study. Int J Solids Struct 2023;262:112053.
[78] Nestler B, Garcke H, Stinner B. Multicomponent alloy solidification: phase-field modeling and simulations. Phys Rev E 2005;71(4):041609.
[79] Schneider D, Schoof E, Tschukin O, Reiter A, Herrmann C, Schwab F, Selzer M, Nestler B. Small strain multiphase-field model accounting for configurational forces and mechanical jump conditions. Comput Mech 2018;61(3):277–95.
[80] Steinbach I, Pezzolla F. A generalized field method for multiphase transformations using interface fields. Physica D 1999;134(4):385–93.
[81] Daubner S, Hoffrogge PW, Minar M, Nestler B. Triple junction benchmark for multiphase-field and multi-order parameter models. Comput Mater Sci 2023;219:111995.
[82] Steinbach I. Phase-field models in materials science. Modelling Simul. Mater. Sci. Eng. 2009;17(7):073001.
[83] Selzer M. Mechanische und strömungsmechanische topologieoptimierung mit der phasenfeldmethode (Ph.D. thesis), Karlsruher Institut für Technologie (KIT); 2014.
[84] Schoof E, Schneider D, Streichhan N, Mittnacht T, Selzer M, Nestler B. Multiphase-field modeling of martensitic phase transformation in a dual-phase microstructure. Int J Solids Struct 2018;134:181–94.
[85] Bekker A, Jimenez-Victory J, Popov P, Lagoudas D. Impact induced propagation of phase transformation in a shape memory alloy rod. Int J Plast 2002;18(11):1447–79.
[86] Amini A, Cheng C, Kan Q, Naebe M, Song H. Phase transformation evolution in NiTi shape memory alloy under cyclic nanoindentation loadings at dissimilar rates. Sci Rep 2013;3(1):3412.